Nuclear analyses for the integration of ITER equatorial Port 2

S. Noce [a,b,*], R. Villari [b], A. Colangeli [b], D. Flammini [b], N. Fonnesu [b], P. Gaudio [a], M. Gelfusa [a], E. Grasso [d], J. Guirao [c], G. Mariano [b,c], F. Mercuri [d], F. Moro [b], A. Previti [b], P. Shigin [c], S. Soro [d], V.S. Udintsev [c], I. Wyss [a]

[a] *Industrial Engineering Department – Via del Politecnico 1, University of Rome "Tor Vergata", Rome 00133, Italy*
[b] *ENEA, Nuclear Department (NUC), Via Enrico Fermi 45, Frascati, Rome 00044, Italy*
[c] *ITER Organization, Route de Vinon sur Verdon, Saint Paul Lez Durance, France*
[d] *LEONARDO Company (branch office France), 595 Rue Pierre Berthier, Aix-en-Provence 13290, France*

ARTICLE INFO

ABSTRACT

The present work is devoted to nuclear analyses in support of the ITER diagnostic Equatorial Port 2 (EP#2) integration. ITER EP #2 is a diagnostic port based on the long-modular Diagnostic Shielding Module (DSM) housing the following systems: Disruption Mitigation System (DMS) in DSM#1 and #3 and X-Ray Crystal Spectroscopy Core (XRCS-Core) in DSM#2. Ensuring adequate radiation shielding is a major challenge since the diagnostic systems require several apertures from the Vacuum Vessel (VV) through the Port Interspace (PI) and up to the Port Cell (PC). In the present study, a three-dimensional MCNP model of EP#2 has been developed, starting from the latest design available from Preliminary Design Review stage (PDR), and successively integrated into the reference 40° ITER C-Model. Comprehensive nuclear analyses have been carried out employing the D1SUNED v3.1.4 code based on the MCNP Monte Carlo transport code. Relevant nuclear quantities during and at the end of plasma operations have been evaluated: i.e., neutron and gamma fluxes and energy spectra along the port from the Diagnostic First Wall (DFW) up to the Bio-Shield Plug (BP), nuclear heating, neutron damage, helium and tritium production, and shutdown dose rate. This analysis allowed the identification of potentially critical areas, and therefore, the implementation of additional shielding options aimed at reducing the neutron streaming and mitigating of the radiation field in the PI region. In this work, the results of the analyses are presented and discussed. Some solutions to mitigate nuclear loads and to improve the shielding in PI area are proposed and their impact has been assessed. Finally, some recommendations for the optimization of the design of EP#2 are provided as well.

1. Introduction

The International Thermonuclear Experimental Reactor (ITER) Equatorial Port (EP) #2 [1] is a diagnostic port under Preliminary Design Review (PDR) stage, based on the long-modular Diagnostic Shielding Module (DSM) [2,3], housing the following systems: Disruption Mitigation System (DMS) [4] in DSM#1 and #3, X-Ray Crystal Spectroscopy Core (XRCS-Core) in DSM#2 [5,6]. Considering the above-mentioned several diagnostics systems, which correspond to several apertures from the Vacuum Vessel up to the Port Cell, one of the main challenges is to ensure sufficient shielding for the radiation field both in Port Cell and Port Interspace. In addition, the assessment of the nuclear loads distributions inside the most radiation exposed regions (e.

g., the in-vessel part) of the Port, plays a key role in the related design activities, such as thermo-structural integrity evaluation, thermo-hydraulic analyses and so on. This work is focused to the generation of the Monte Carlo N-Particle (MCNP) [7] model of in and ex-vessel components (up to the Bio-Shield Plug (BP)) of EP#2 based on the latest design system available (see Figs. 1–3) and to the nuclear analysis performed with D1SUNED-v3.1.4 code and the reference dataset [8,9] based on the MCNP Monte Carlo transport code. Neutron and prompt photon flux, nuclear heating, radiation induced damage, tritium and helium concentration at ITER End Of Life (EOL) have been calculated in the in-vessel Port Plug (PP) area. Furthermore, considering the ex-vessel section; neutron flux and spectra during operation as well as Shutdown Dose Rate (SDDR) variation in Port Interspace (PI) relevant
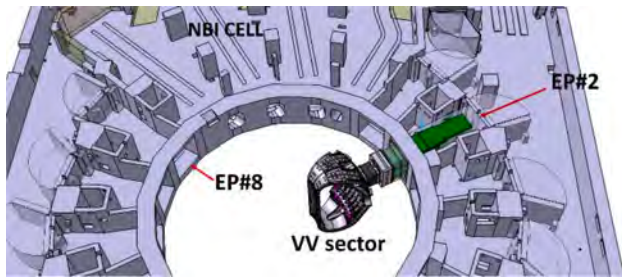

Fig. 1. Top view of the ITER equatorial sector.
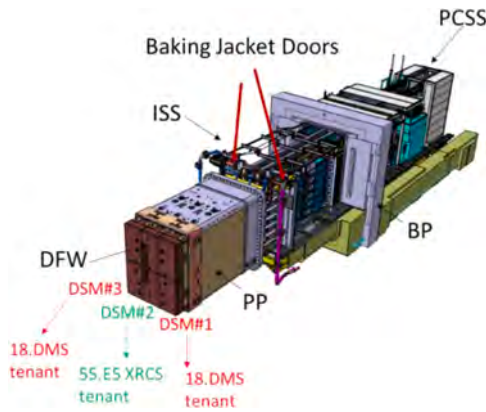
Fig. 2. Equatorial Port #2 system (front view).
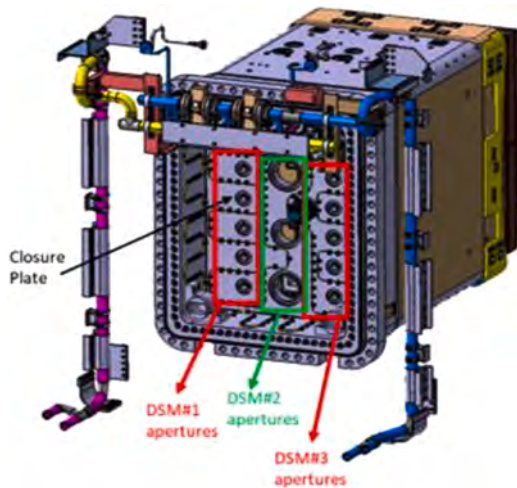
Fig. 3. Equatorial Port Plug #2 system (back view).

Fig. 4. Plot of the MCNP C-model of ITER with integrated EP#2 system (ZX section at PY −40, DSM#1 view).

Fig. 5. Plot of the MCNP C-model of ITER (top) and equivalent neutronic CAD model (bottom) with integrated EP#2 system (YX section at PZ 80).

workstations (WS) at 10^6 s at the end of SA2 scenario [10] have been calculated, both with the baseline design and also with an additional shielding system located in the Interspace Support Structure (ISS) region, aimed to mitigate the ex-vessel radiation field.

2. Details of the calculations

The generation of the model includes simplifications, conversion from Computer-Aided Design (CAD) model to MCNP and integration in the ITER reference MCNP C-model. The neutronics model has been prepared through a pre-processing of CAD files using the Ansys/SpaceClaim 2022 [11] software. The simplification procedure is performed to enable automatic conversion, as some complex geometries and high-order surfaces cannot be converted by the software.
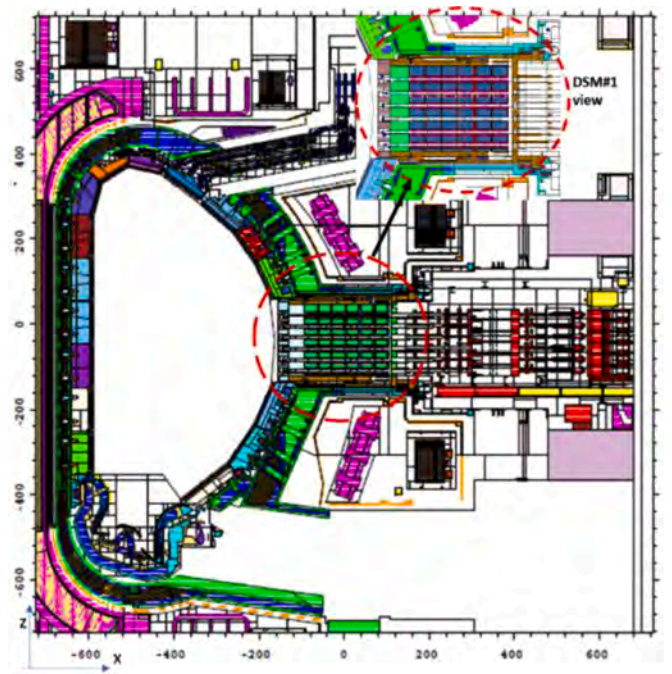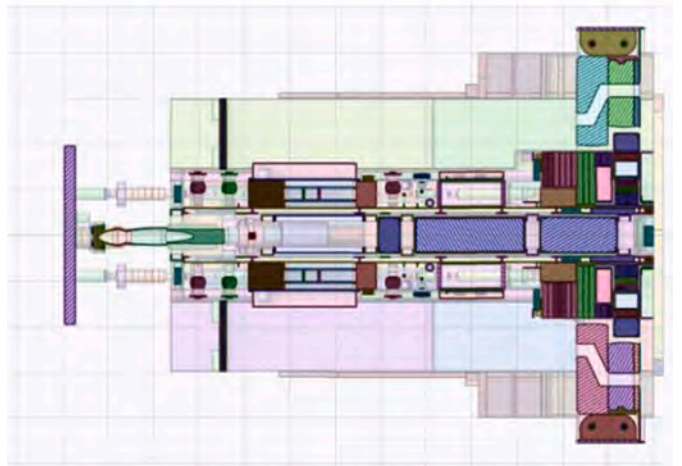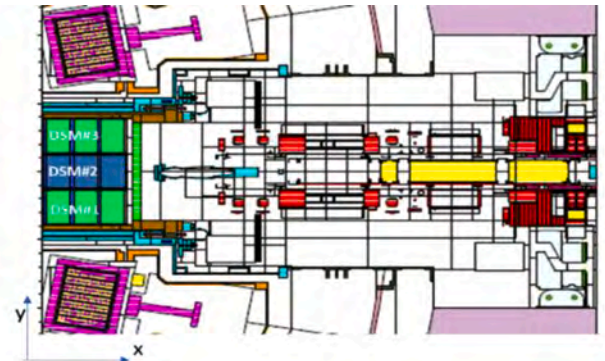
Furthermore, many small details such as bevels, nuts, threading of the bolts are unnecessary [12,13] for the nuclear analysis and they have been removed. In addition, a homogenous representation of the
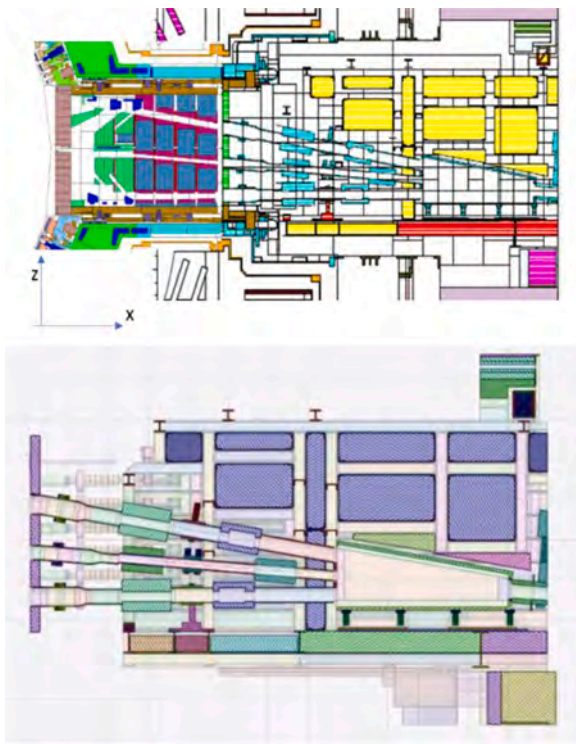
Fig. 6. Plot of the MCNP C-model of ITER (top= and equivalent neutronic CAD model (bottom) with integrated EP#2 system (ZX section at PY 0 – DSM#2 view).
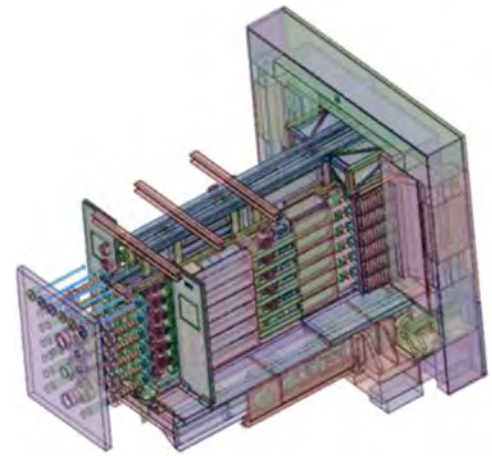

Fig. 8. Ex-vessel neutronic CAD baseline (no additional shielding) model.
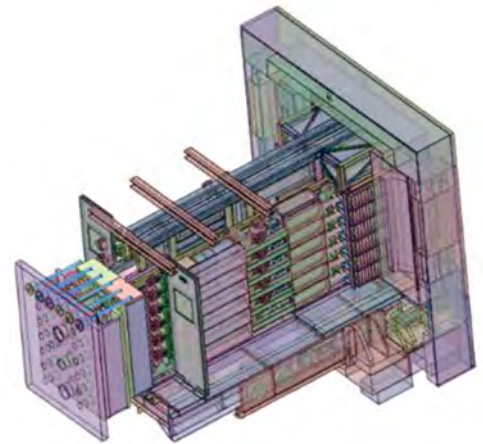

Fig. 9. Ex-vessel neutronic CAD model with additional shielding arranged immediately after the closure plate.
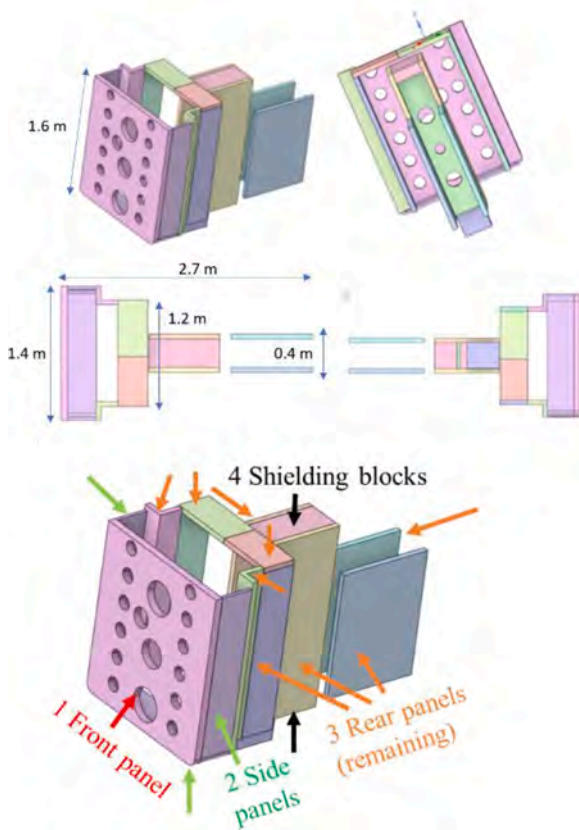

Fig. 7. Additional shielding configuration for the EP#2 ISS region: front view (top left), back view (top right), upper view (central left), lower view (central right) + Additional ISS shielding panels classification (bottom).

shielding trays inside the DSMs, the Diagnostic First Wall (DFW) modules has been preferred considering the PDR phase of the EP#2 system in order to simplify and speed up the modelling phase. The neutronic CAD obtained after the simplifications, aimed to preserve the volume difference within 2%, has been converted to the MCNP geometry with SUPERMC 3.4.0 [14] code. Finally, the MCNP model of EP#2 has been validated and integrated [15,16] into the EP#8 PDR reference 40° ITER C-model [17–19], keeping unvaried the adjacent sectors [18] and recycling some generic parts from EP#8 system. Albeit this is not the exact position for EP#2 (see Fig. 1, Figs. 4, 5 and 6), this decision can be in principle justified in terms of methodology and results expected for the PDR stage, by the fact that both of them cannot be significantly affected by this integration choice. In addition, the necessity to speed up and simplify the final model preparation, leads to consider this choice as appropriate. The integration in the proper ITER sector to perform more accurate nuclear analysis including cross-talk with surrounding ports is foreseen for the next design phase of Final Design Review - FDR.

In addition to the baseline design (see Figs. 2 and 8), to improve the radiation shielding of the most exposed area of the port interspace where workers can operate, an additional shielding configuration consisting of several panels which will be better described later, has been implemented with the designers in the ISS region, close to the Closure Plate (see Figs. 7 and 9).

The radiation transport calculations have been performed with D1SUNED v3.1.4 rev.2 code [8,9], using FENDL3.1d [20] and
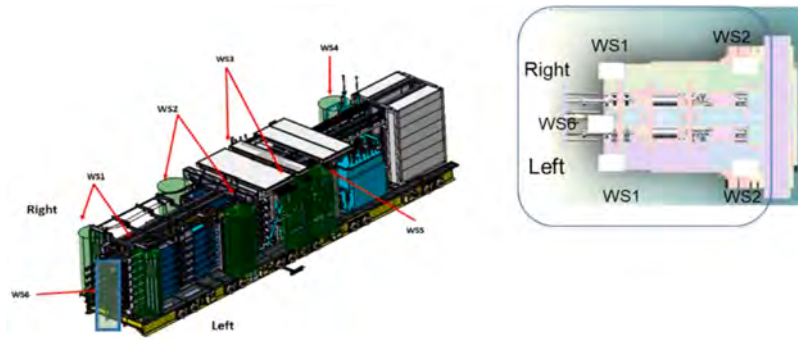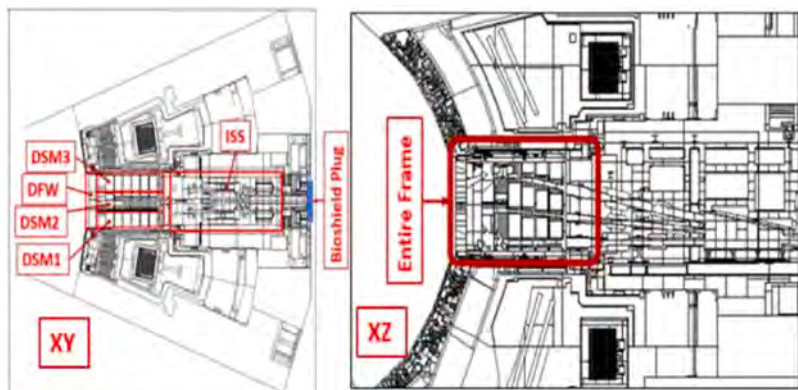
Fig. 10. EP#2 Workstation positions.

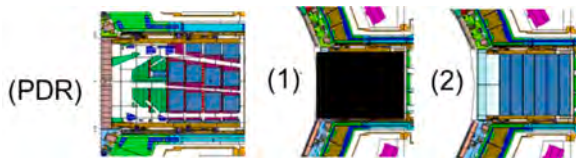**Fig. 11.** Mesh tally for neutron spectra calculations.

Fig. 12. Additional configurations examined to study the central drawer in-vessel components contribution: DSM#2 ideal radiation blind (1) and DSM#2 full shield – no penetrations (2).

MCPLIB84 [21] nuclear data libraries of neutrons and photons transport, respectively. D1SUNED computational tool have been used on CRESCO6 cluster [22] in mode PRMPT for generation of prompt photons from nuclear interactions. Weight windows file has been generated by means of ADVANTG code [23] to ensure the statistical significance of the computed nuclear responses. Calculations have been performed by running up to 2×10^{11} histories. Standard ITER Deuterium-Tritium Plasma Source description included in C-model has been used for the simulations.
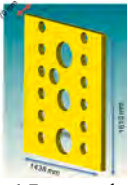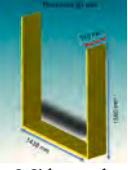
3. Nuclear analyses

The following quantities have been calculated with cell-based and/or mesh tallies:

- integral nuclear heating and average nuclear heating density on in-vessel EP#2 components, using cell-based tallies.

- Spatial distribution ($2 \times 2 \times 2$ cm^3 voxel mesh) from the Diagnostic First Wall (DFW) to the Closure Plate (CP) of: neutron flux, prompt photon flux, nuclear heating density, radiation induced damage (displacement per atom – dpa) in steel and copper at EOL, helium production at EOL, tritium production at EOL.
- Neutron flux distribution along the equatorial port, from the plasma to the bio-shield plug in a mesh of $10 \times 10 \times 10$ cm^3 voxels.
- Neutron flux in maintenance workstations with cell-based and single voxel mesh tallies. The positions of the relevant workstations are shown in Fig. 10. It should be noted that, although workstations #3, #4 and #5 have been considered as input request, this study is focused on nuclear analyses up to the Bio-Shield Plug only; therefore, these maintenance locations have been not taken into consideration during this design phase.
- Neutron spectra in 175 VITAMIN-J energy group structure in single voxel meshes accordingly to Fig. 11.
- Comparison and calculation of %variation of the SDDR at 10^6 s of cooling time after SA-2 irradiation scenario, in maintenance work-stations with the aim to identify the contribution due to the in-vessel design of the central drawer and the impact of its openings. This comparison is between baseline configuration and two "dummy" configurations (Fig. 12): (1) "ideal" refers to a configuration in which all neutrons and gamma passing through the central drawers (DSM#2) are inhibited and, consequently, there is no gamma generation behind DSM#2 which can be considered as radiation transport "blind", (2) the second configuration refers to fully shielded drawers without any penetration (namely "full") where the DSM#2 shielding trays mixture is extended in the whole available volume (no penetrations).

Table 1
ISS additional shielding panels material's mixtures, considering several cases.

Shield Shielding component	Material mixtures (%Vol.)			
	Case#1 a&b	Case#2 a&b	Case#3	Case#4
1 Front panel	1.8% SS-IG 84% Pyrogel 14.2% Flexi-Boron ρ (g/cm³) = 0.54		3% SS-IG 68.7% Pyrogel 28.3% Flexi-Boron ρ (g/cm³) = 0.84	
2 Side panels 3 Rear panels	4.1% SS-IG 62.8% Pyrogel 33.1% Flexi-Boron ρ (g/cm³) = 0.99		16% SS-IG 20% Pyrogel 18% AlBor (95% ¹⁰B) 46% Flexi-Boron ρ (g/cm³) = 2.55	16% SS-IG 20% Pyrogel 18% AlBor (95% ¹⁰B) 40% Flexi-Boron 6% Pb ρ (g/cm³) = 3.13
	a 10% SS-IG 40% Pyrogel 20% **AlBor (nat B)** 30% Flexi-Boron ρ (g/cm³) = 1.90 b 10% SS-IG 40% Pyrogel 20% **AlBor (95% ¹⁰B)** 30% Flexi-Boron ρ (g/cm³) = 1.90	a 10% SS-IG 40% Pyrogel 16% **AlBor (nat B)** 30% Flexi-Boron 4% Pb ρ (g/cm³) = 2.25 b 10% SS-IG 40% Pyrogel 16% **AlBor (95% ¹⁰B)** 30% Flexi-Boron 4% Pb ρ (g/cm³) = 2.25		
4 Shielding blocks	80% Heavy Borated Concrete 20% SS-IG ρ (g/cm³) = 4.47			

- Comparison and calculation of %variation of the SDDR at 10^6 s of cooling time after SA-2 irradiation scenario, in maintenance workstations between baseline and additional ISS shielding configurations. For this assessment, several cases varying the material mixtures composition for each shielding panels (Figs. 7 and 9) have been investigated (Table 1).

The nuclear heating has been calculated by scoring the energy released by neutrons and prompt photons. To this purpose a track length estimator with proper multipliers taking into account the neutron yield, and the numbers which identify the total cross section and the heating number depending on the material considered, has been used for mesh tallies, while inbuild energy release has been used for cell-based tallies. This is performed separately for neutrons and photons. The NRT model has been used for radiation induced damage in displacement per atom [24,25], using 40 eV as energy threshold of iron for the steel. The neutron and photon fluxes and the nuclear heating have been normalized to 500 MW of fusion power (1.973×10^{19} n/s in 40° sector). The

cumulated quantities (damage, helium and tritium concentration) have been calculated at ITER EOL, considering 4700 h of operation at 500 MW of Fusion Power (3.338×10^{26} n in 40° sector). The D1SUNED input has been settled to perform simulations of neutrons and decay gammas, with proper settings and data libraries [8,9]. The decay gammas are generated from 122 activation reactions due to 80 parent nuclides.

The coupled simulations of neutron and decay gammas have been performed with a "local" approach. All the upper, lower and adjacent equatorial ports of C-model envelopes are voided and set to zero importance for neutron and photon (i.e., to prevent neutron and photon transport and generation in other ports) to provide the neutron fluxes and SDDR distributions by excluding the impact of the cross-talk with the other ports, which are not consistent with actual EP#2 location in the ITER machine.

The results obtained in local approach underestimate the SDDR level expected in full environment, thus the configurations exceeding the SDDR target in local approach need for shielding design optimization.

The statistical uncertainty distribution maps are shown for neutron and photon flux, for nuclear heating density in steel, damage in steel and for tritium and helium concentration in Fig. 13. Statistical uncertainty of the neutron flux is below 5% in the whole map, except for an extremely limited zone. Photon flux present some few voxels inside the EPP with statistical uncertainty around 20% and localized hotspot above this value that are inside the apertures' channels and outside the EPP, as for the nuclear heating density and damage in steel error maps. The most critical situation is found for tritium and helium concentration. The regions with statistical uncertainty larger than 20% are however localized where the tritium and helium concentration is very low. These acceptable errors distributions are confirmed also looking at the neutron flux uncertainty maps covering the whole system as shown in Fig. 14. All the necessary neutronics recommendations for ITER nuclear analyses, as well as, the materials compositions have been accurately followed in accordance with ITER guidelines and specifications [12,13,26,27].

4. In-vessel analysis results

Neutron and Photon flux

Neutron and photon flux inside the EPP#2 have been calculated with a $2 \times 2 \times 2$ cm³ voxels meshes. Neutron flux is around $2 \bullet 10^{14}$ n/cm²/s at the FW and it decreases to more than $5 \bullet 10^8$ n/cm²/s behind the CP, similarly to photon flux, which varies from circa $3 \bullet 10^{14}$ γ/cm²/s close to the FW (peak value) up to $5 \bullet 10^8$ γ/cm²/s after the CP. These values can be found in the radiation maps, shown in Figs. 15 and 17 for $y = 0$ cm as cut view (respectively for neutrons and photons), and Figs. 16 and 18 (respectively for neutrons and photons), in correspondence of $z = 50$ cm cut (this one is corresponding to a position at 4 cm behind the CP). Behind the CP significant radiation (both neutrons and photons) streaming is found around the PP walls (peaked at approximately 10^9 n/cm²/s and 10^9 γ/cm²/s), in correspondence of the six apertures (both on right and left side) of DMS DSM#1 and #3 and at the three central apertures of XRCS-Core of DSM#2 (peaked at approximately $5 \bullet 10^9$ n/cm²/s and 10^9 γ/cm²/s).

Integral nuclear heating and nuclear heating density

Integral nuclear heating and average nuclear heating density have been calculated with cell-based tallies. Cells were grouped by components and energy deposition from neutrons and photons has been tallied. The results of EPP#2 components have been subdivided into the three DSMs (#1, #2 and #3). The nuclear heating contribution on PP structure, water services and other external components is not included in these calculations. The results of the nuclear heating density on structural parts of DSM#1, DSM#2, DSM#3 and the related break-downs are
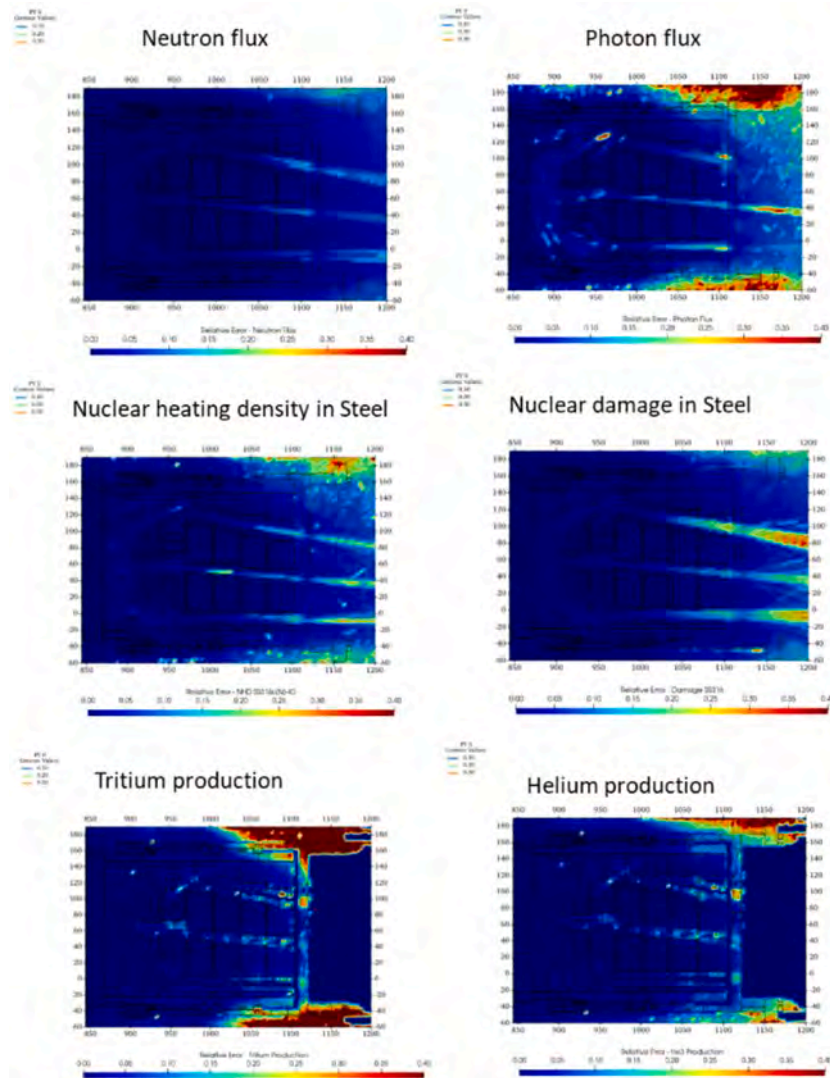
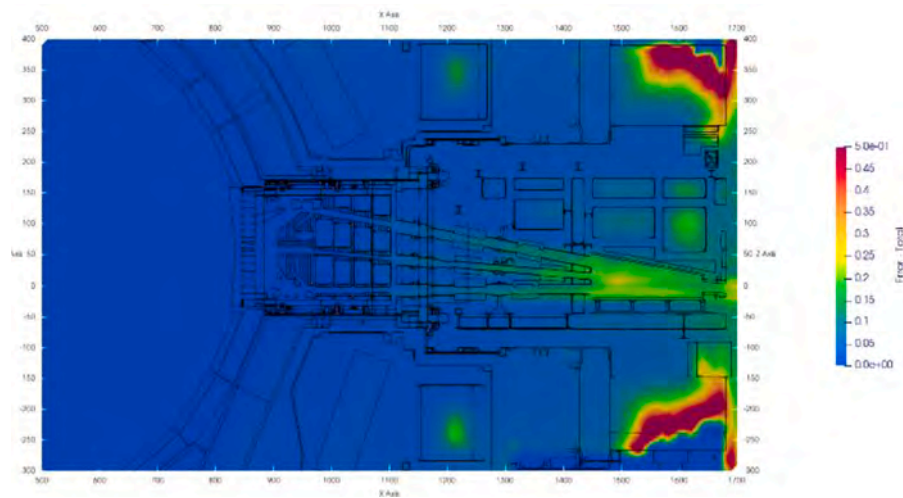**Fig. 13.** Statistical uncertainty for radiation maps (view at PY 0).

Fig. 14. Statistical uncertainty for neutron flux map covering both in-and ex-vessel parts (view at PY 0).
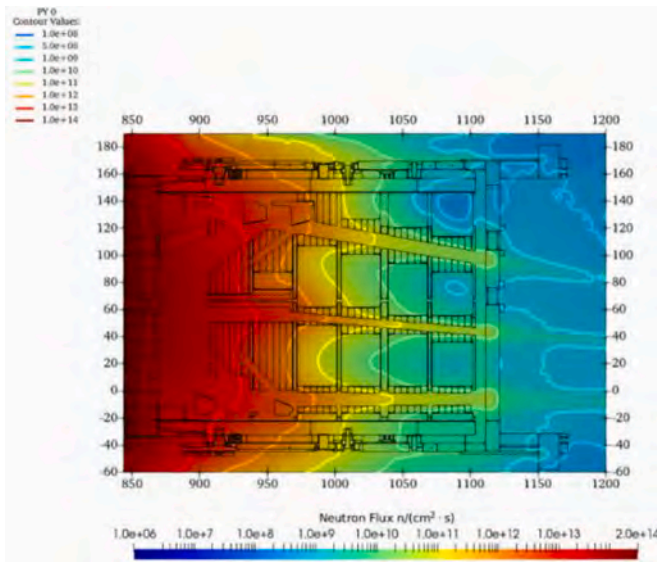
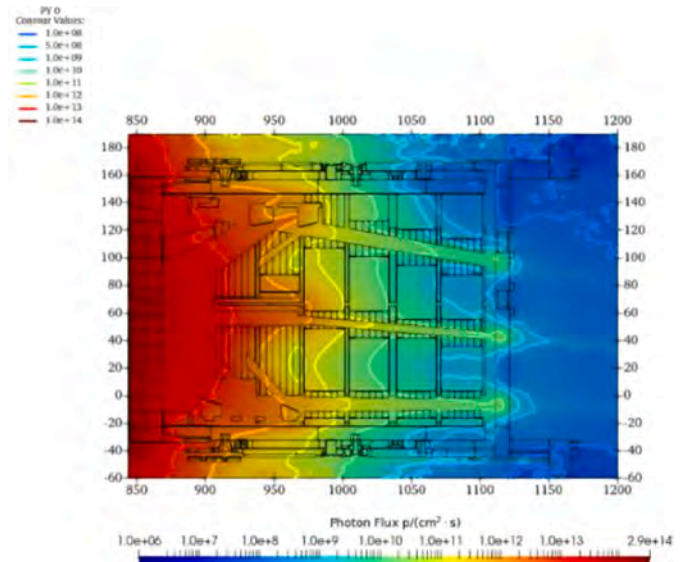**Fig. 15.** Neutron flux map at PY 0 (along DSM#2).

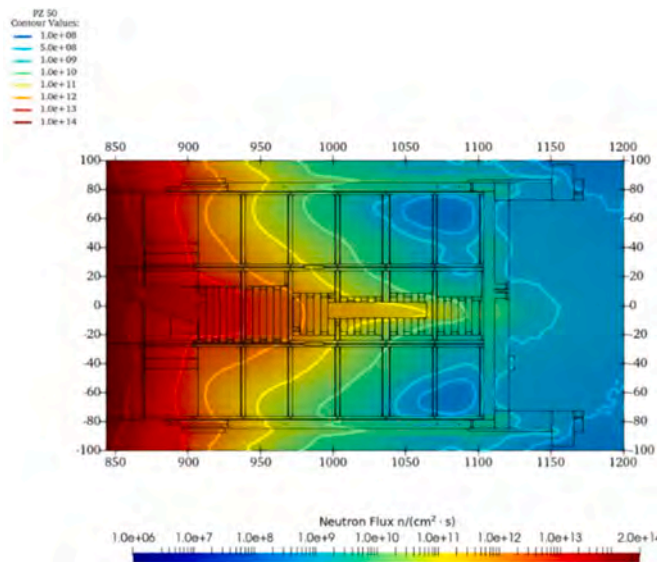**Fig. 17.** Photon flux map at PY 0 (along DSM#2).

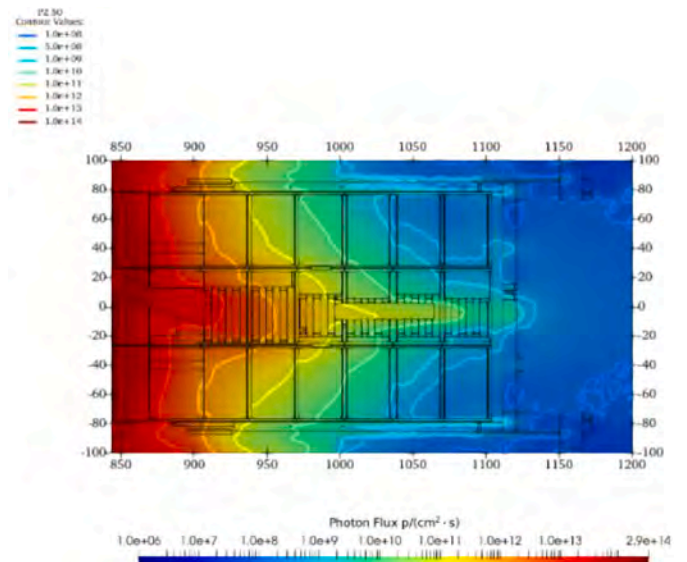**Fig. 16.** Neutron flux map at PZ 50.

Fig. 18. Photon flux map at PZ 50.

shown in Figs. 19–21, respectively. Statistical uncertainty is well below 1% for all components, with exception of the very small and well shielded ones (which achieve statistical errors of 3% as maximum).

As a result, a total nuclear power deposition on the three EPP#2 DSMs (not including PP structure) of 2.3 MW has been calculated. Most of the power (about 80%) is deposited on the DFW structure. DSMs' structure accounts for about the 18% of the total power. Among the diagnostic systems, the highest loads are on the DMS shutter injectors of DSM#1 and #3 with a total power of around 32 kW (just over 1% of total). All other components have a contribution to the total nuclear heating less than 1%.

Nuclear heating density maps have been calculated with a resolution of $2 \times 2 \times 2$ cm^3 over the whole EPP#2 and include the contribution of energy deposited by neutrons and photons. The calculations have been performed considering a proper multiplier, directly providing the nuclear heating density considering the materials and densities inside the voxels as defined in the MCNP model.

Figs. 22 and 23 show bi-dimensional radial-poloidal ($y = 0$ cm) nuclear heating density maps for SS316L(N)-IG, and CuCrZr-IG respectively. The peak value for nuclear heating density in SS is around 7.1 W/cm^3 at the FW and decreases up to 10^{-5} W/cm^3 and below at the rear flange. The peak value in Back Fillings blocks of DSM#2 are 0.93 W/cm^3 on columns C1 and 0.2 W/cm^3 on columns from C2 to C6 (see Fig. 27). High nuclear heating is found in DMS Shutter Injectors made of CuCrZr-IG (peak 6.8 W/cm^3) as shown in Fig. 24 and on the most exposed B$_4$C bricks in DSM#2 (peak 1.8 W/cm^3) as shown in Fig. 29.

Furthermore, this nuclear heating analysis has contributed to update the design of DSM#2 SS316L(N)-IG shielding column C1 to avoid nuclear heating hotspots on the mostly exposed B$_4$C bricks, w/o compromise shielding performance. In fact, looking at Fig. 25, it isevident a

Components - DSM#1	Mixture (%Vol.)		V (cm³)	Average nuclear heating density (W/cm³)	Nuclear power deposited (kW)
DFW	SS316L(N)-IG	85.00%	174655	3.43E+00	598.33
DFW Fix. Systm.	SS316L(N)-IG	100.00%	11283	3.88E-01	4.38
Neutron Stoppers	SS316L(N)-IG	100.00%	6165	2.16E-03	0.01
Back Fillings	SS316L(N)-IG	100.00%	126425	5.23E-03	0.66
18-DM Shutter Injectors	CuCrZr-IG	100.00%	4633	3.25E+00	15.05
Vertical Plates 1-5	SS316L(N)-IG	98.00%	111616	1.64E-02	1.83
Vertical Plates 6	SS316L(N)-IG	100.00%	19609	1.00E-05	1.97E-04
Vertical Drawer	SS316L(N)-IG	91.00%	276886	3.70E-01	102.33
Shielding Trays	SS316L(N)-IG	11.27%	155494	4.84E-03	0.75
	B4C	43.13%	595073	7.03E-03	4.18
Top and Bottom Drawer	SS316L(N)-IG	100.00%	232088	8.17E-02	18.97
Generic Parts	Steel 660	100.00%	8950	7.87E-03	0.07
	AlBr	100.00%	8033	1.05E-02	0.08

Fig. 19. Results for integral nuclear heating and average nuclear heating density in DSM#1 EPP #2 components.

Components - DSM#2	Mixture (%Vol.)		V (cm³)	Average nuclear heating density (W/cm³)	Nuclear power deposited (kW)
DFW	SS316L(N)-IG	85%	168918	3.62E+00	612.31
DFW Fix. Systm.	SS316L(N)-IG	100%	11285	5.26E-01	5.94
Neutron Stoppers	SS316L(N)-IG	100%	12193	1.78E-03	2.18E-02
Back Fillings C1	SS316L(N)-IG	91%	140365	1.84E-01	25.76
Back Fillings C2	SS316L(N)-IG	100%	96284	1.98E-02	1.91
Back Fillings C3-C6 (other)	SS316L(N)-IG	100%	169209	2.51E-03	0.42
E5 Xray Spectrometer	SS316L(N)-IG	100%	15140	4.02E-02	6.09E-01
E5 Xray Spectrometer	CuCrZr-IG	100%	16270	2.08E-01	3.39
E5 Xray Spectrometer	SS316L(N)-IG	91%	15880	1.42E-01	2.26
Vertical Plates 1-5	SS316L(N)-IG	98%	96816	1.01E-02	0.98
Vertical Plates 6	SS316L(N)-IG	100%	12369	3.06E-05	3.79E-04
Vertical Drawer	SS316L(N)-IG	91%	181766	6.32E-01	114.96
Shielding Trays	SS316L(N)-IG	14%	134786	4.18E-03	0.56
	B4C	42%	393967	9.78E-03	3.85
Top and Bottom Drawer	SS316L(N)-IG	100%	229404	7.50E-02	17.21
Generic Parts	Steel 660	100%	9442	2.55E-02	0.24
	AlBr	100%	8106	1.74E-02	0.14

Fig. 20. Results for integral nuclear heating and average nuclear heating density in DSM#2 EPP #2 components.

Components - DSM#3	Mixture (%Vol.)		V (cm³)	Average nuclear heating density (W/cm³)	Nuclear power deposited (kW)
DFW	SS316L(N)-IG	85.00%	174655	3.51E+00	613.62
DFW Fixation Systems	SS316L(N)-IG	100.00%	11283	4.55E-01	5.13
Neutron Stoppers	SS316L(N)-IG	100.00%	6165	1.12E-03	0.01
Back Fillings	SS316L(N)-IG	100.00%	126425	4.61E-03	0.58
18-DM Shutter Injectors	CuCrZr-IG	100.00%	4633	3.48E+00	16.11
Vertical Plates 1-5	SS316L(N)-IG	98.00%	111616	1.06E-03	0.12
Vertical Plates 6	SS316L(N)-IG	100.00%	19609	1.21E-05	2.38E-04
Vertical Drawer	SS316L(N)-IG	91.00%	276886	4.10E-01	113.45
Shielding Trays	SS316L(N)-IG	11.27%	155494	4.27E-03	0.66
	B4C	43.13%	595073	5.93E-03	3.53
Top and Bottom Drawer	SS316L(N)-IG	100.00%	232088	8.26E-02	19.18
Generic Parts	Steel 660	100.00%	8950	1.85E-02	0.17
	AlBr	100.00%	8033	1.05E-02	0.08

Fig. 21. Results for integral nuclear heating and average nuclear heating density in DSM#3 EPP #2 components.

direct neutron irradiation exposure of the first B_4C bricks rows due to both the huge DFW penetration, needed as line of sight for the tenant XRCS-Core function (which cannot be changed) and also to a not complete shielding offered by the back-filling shielding column C1 starting design, on the most exposed bricks. This leads to several localized and intense nuclear heating peaks up to 16 W/cm^3 (see Fig. 26) which implies risky thermal hotspots on the steel structural parts surrounding the B_4C bricks. To avoid this drawback, a new DSM#2 shielding column C1 design has been proposed by the port integration team designers (see Figs. 27 and 28) and integrated in the reference MCNP neutronic model of this study, thus leading to a new B_4C bricks configuration which allows to achieve a heating peaks reduction of a factor 10 (Fig. 29).

Radiation induced in steel and copper damage at EOL

Radiation induced damage maps have been calculated with a resolution of $2 \times 2 \times 2$ cm^3 over the whole EPP#2 on Steel 316L(N)-IG for and Copper. Damage is given in terms of dpa at EOL (i.e., 4700 h at full-power operations). Fig. 30 shows bi-dimensional radial-poloidal ($y = 0$ cm) radiation damage maps for SS316L(N)-IG. Fig. 31 shows bi-dimensional radial-toroidal ($z = 120$ cm) radiation damage maps for copper. The maximum cumulated damage in steel and copper is around 2.5 dpa and 3.8 dpa at the FW, respectively. Both damage in steel and copper decreases up to 10^{-5} dpa and below at the closure plate regions even if in some location it results greater than 10^{-4} dpa. This especially occurs close to the streaming paths because damage is very sensitive to the high energy part of the spectrum.

Tritium concentration and helium production at the EOL

Tritium concentration and helium production have been calculated at ITER EOL. The calculation has been performed with a $2 \times 2 \times 2$ cm^3 resolution mesh over the whole EPP#2, and results are given in terms of gram of tritium per cubic centimetres and atoms part per million (appm)

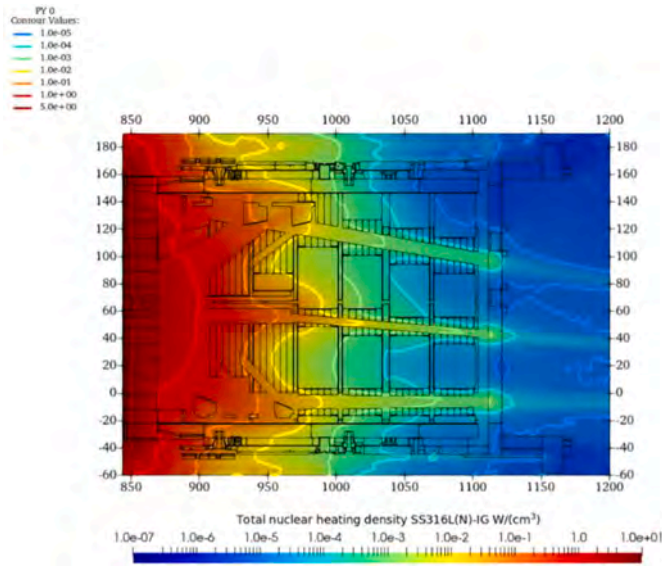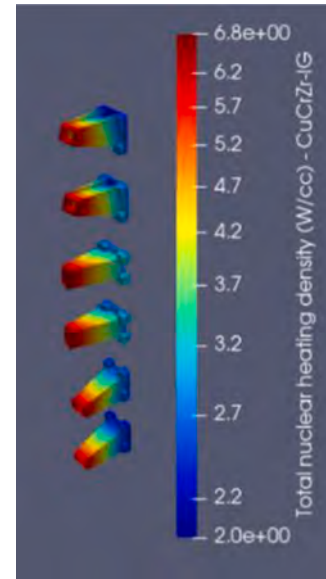**Fig. 22.** Nuclear heating density on SS316L(N)-IG at PY 0.

Fig. 23. Nuclear heating density on CuCrZr-IG at PY 0.

Fig. 24. Nuclear heating density distribution on 18-DM Shutter Injectors (DSM #1 and #3).
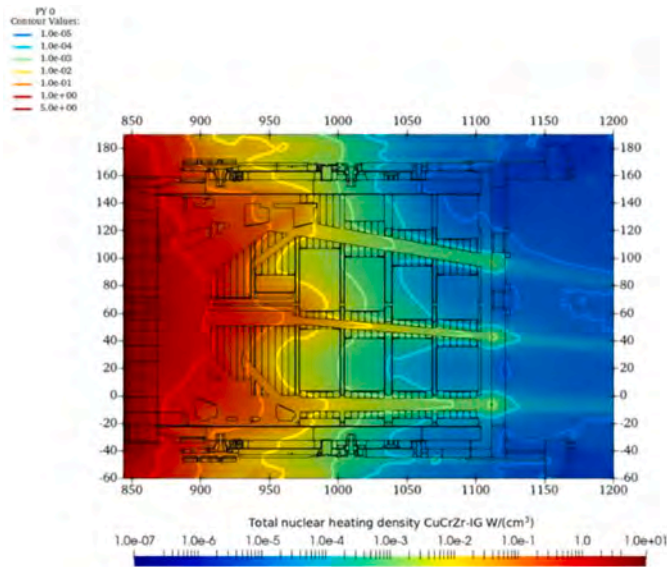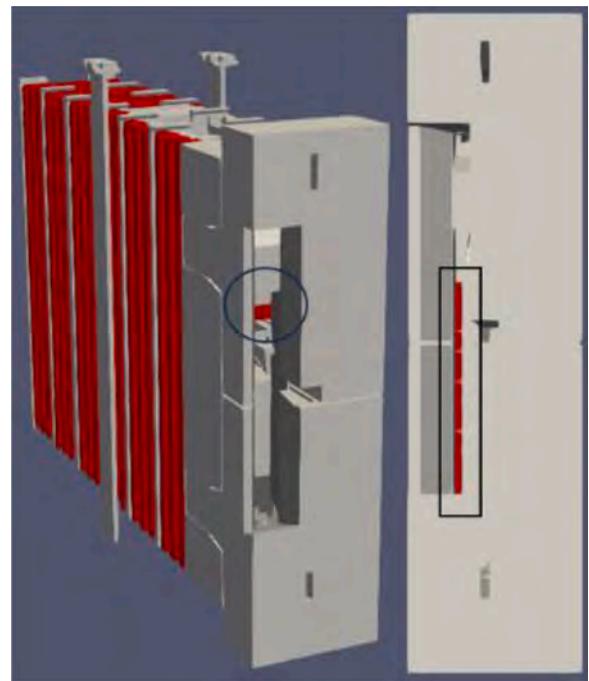

Fig. 25. B$_4$C bricks of DSM#2 (highlighted in red) having a direct view on neutrons from plasma due to the huge DFW penetration.

for He. Fig. 32 shows bi-dimensional radial-poloidal ($y = -15$ cm) tritium concentration map. Fig. 33 shows bi-dimensional radial-toroidal ($z = 50$ cm) tritium concentration map.

The largest value is around $4.4 \cdot 10^{-8}$ g/cm^3 found in the B$_4$C of first shielding tray column. It decreases up to approximately $1 \cdot 10^{-11}$ g/cm^3 in the last shielding tray column. In general, the largest amount of tritium is produced inside Boron Carbide elements, while structural elements results in a lower production of tritium. In DFW mixture it is about $5 \cdot 10^{-9}$ g/cm^3 and at the closure plate is below 10^{-12} g/cm^3. This very low value of tritium concentration leads to larger statistical uncertainty in some regions of the distribution maps. Both (n,^{4}He) and (n,^{3}He) reactions have been considered in the calculations of He production. The largest amount of He production is found in the B$_4$C of the shielding trays in the first columns and in the DFW mixture with a value of around 40 appm which decreases below 10^{-4} appm at the CP. Figs. 34 and 35 show the He production maps in a horizontal ($z = 50$ cm) and vertical ($y = -15$ cm) cut of EPP#2 are shown.

5. Ex-vessel analysis results

Neutron flux and spectra

Neutron flux along EPP#2 has been calculated with a $10 \times 10 \times 10$ cm^3 voxels meshes. Figs. 36-41 show the 3D maps of neutron flux distribution for various sections of interest with contour at 10^8 n/cm^2/s. The statistical error is well below 10% in the zone of interest (see Fig. 14). In Figs. 36-38, it is possible to distinctly observe a noteworthy neutron streaming resulting from the penetrations. Notably, the neutron flux level surpasses 10^9 n/cm^2/s at the bio-shield along the opening.

Fig. 37 shows the neutron flux distribution maps along DSM#1 and #3. In comparison to DSM#2, the streaming effect from DSM#1 and
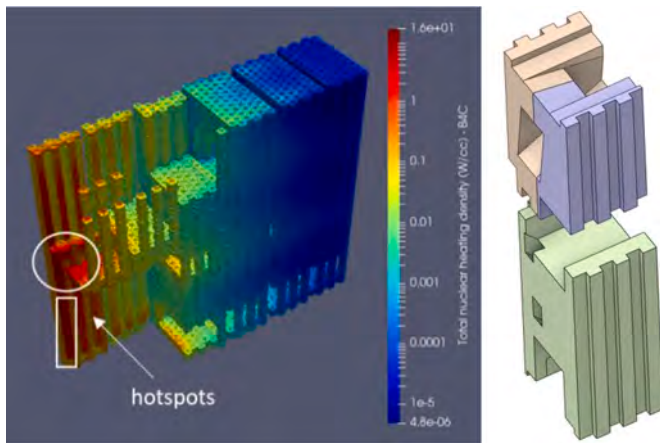
Fig. 26. Nuclear heating density map resampled on the starting B₄C bricks configuration of DSM#2 (on the left) with the starting shielding column C1 design (on the right).
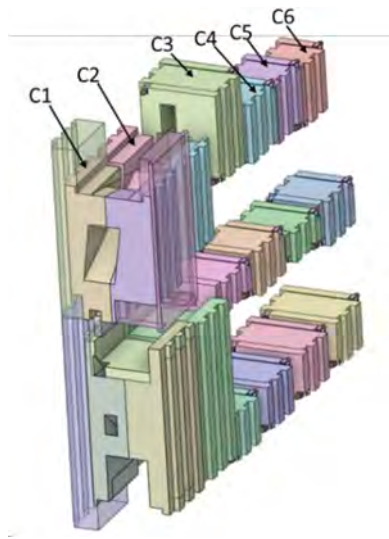

Fig. 27. Starting DSM#2 shielding columns back-filling (from C1 to C6), and the new C1 design overlapped in transparency.

Fig. 28. Nuclear heating density map resampled on the starting configuration of B₄C bricks of DSM#2 with the overlapping of the new shielding column C1 design.

Fig. 29. Nuclear heating density map resampled on the final B₄C bricks configuration of DSM#2 (on the left) with the new shielding column C1 design (on the right).

DSM#3 penetrations is less pronounced and concentrate itself closer to the closure plate. Nonetheless, it still constitutes an additional source of streaming that requires mitigation. The above-mentioned observations are more evident through the investigation of the radial toroidal maps along the XRCS-Core (bottom) and DMS penetrations (top) compared to maps in the middle EP (central) reported in Figs. 38, 40 and 39, respectively. After 1400 cm the neutron flux level is generally lower than 10^8 n/cm²/s except for the area behind the central opening (Fig. 41, c and d). In particular, behind the bio-shield plug (d) the neutron flux level is generally lower than 10^6 n/cm²/s, except for the central and bottom area. The contour at $6 \cdot 10^4$ n/cm²/s is also shown. Even if the present study does not include the Port Cell, it is anyway useful to preliminarily identify the zone where the design limit for the protection of the electronic components is satisfied. The neutron flux distribution behind the closure plate, in the ISS region (middle of WS#1 and #2) and behind the bio-shield plug are shown in Fig. 41.

Fig. 42 shows the neutron spectra in EP#2 components and the related average neutron fluxes are listed in Table 3. It is evident the neutron spectra and related average neutron fluxes attenuation, coming from the most exposed components to the plasma (DFW, DSMs and PP frame) up to ISS 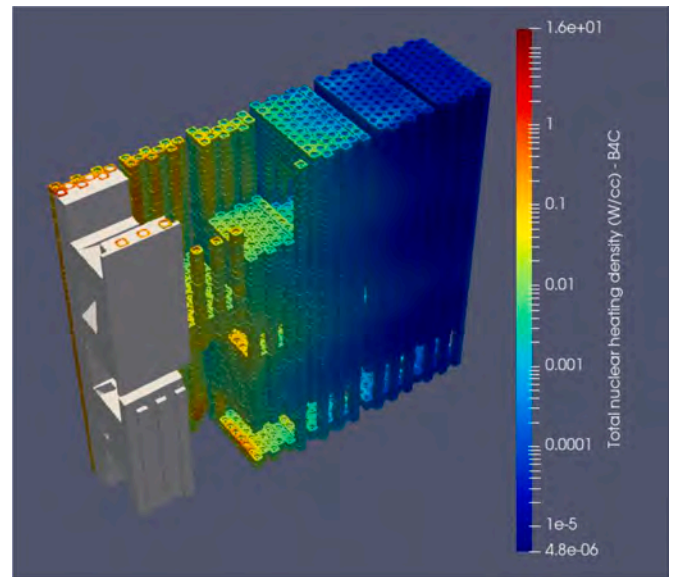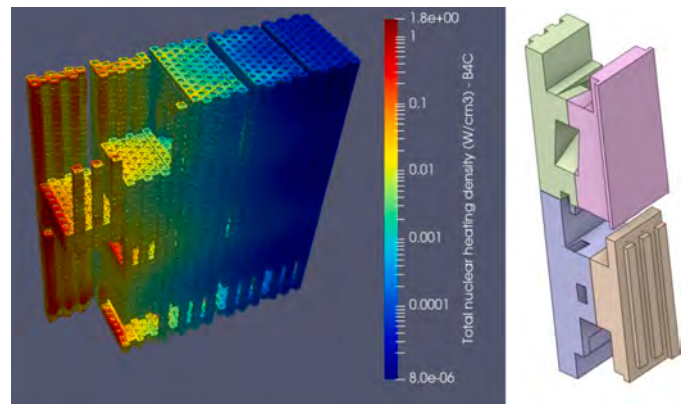and bio-shield plug, as it is reasonable to expect. The average neutron fluxes for the workstations shown in Fig. 10, are listed in Table 2. The neutron flux in DSMs is about 1.5 order of magnitude lower than in DFW. In DSM#2, a higher neutron flux has been found, compared to DSM#1 & #3. The neutron flux in ISS is an order of magnitude higher with respect to bio-shield plug. The neutron flux in the left workstations is higher compared to the right ones. The ratio between WS#1 and WS#2 is 6.6.

SDDR %variation, comparison between several configurations and mitigation strategies implemented

This section is devoted to analysing the impact of several contributions and additional configurations to shutdown dose rate at 12 days after shutdown in PI. In particular, the following assessments are related to SDDR in WS#1 and WS#2 (left and right averaged) as shown in Fig. 10.

Considering the baseline configuration, the following statements can be supported:

- As expected, the SDDR in workstations #1 is higher than workstations #2, clearly due to the closest position to plasma neutron source and in-vessel penetrations. Anyway, the SDDR reduction between
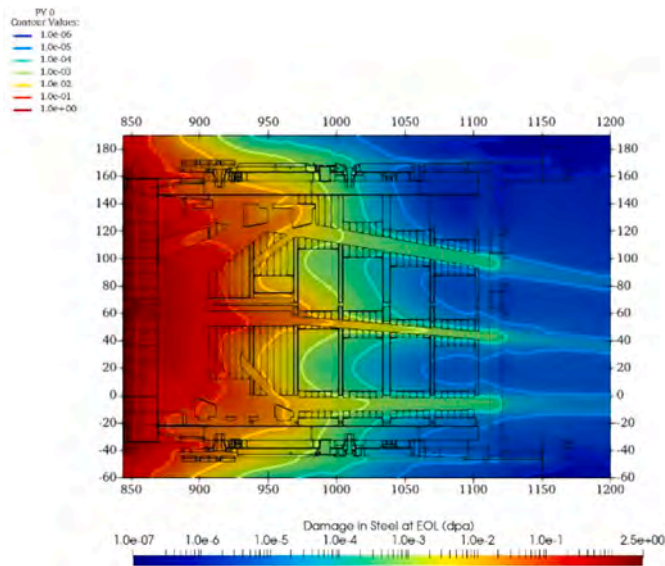
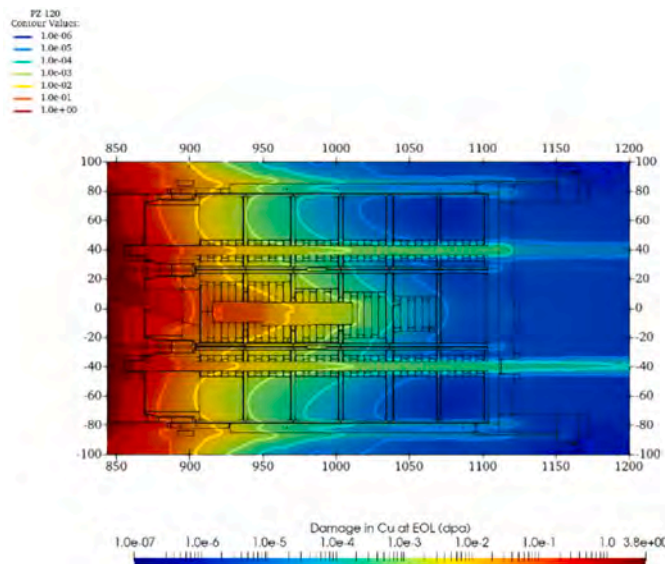**Fig. 30.** Damage in SS316L(N)-IG at PY 0 (along DSM#2).

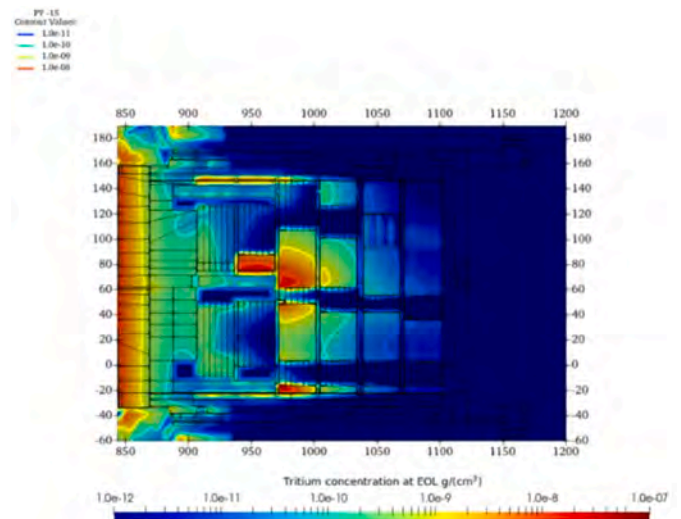**Fig. 32.** Tritium production at EOL in PY −15 (DSM#2).
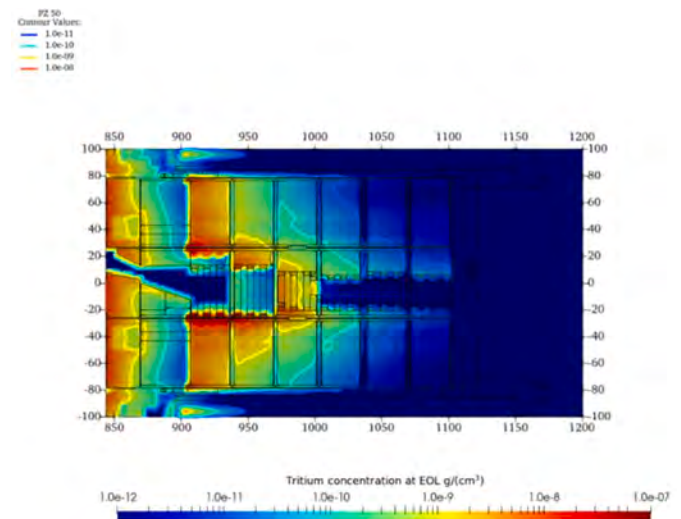

Fig. 31. Damage in Copper at PZ 120.

Fig. 33. Tritium production at EOL in PZ 50.

WS#1 and WS#2 is of the order of 90% (both left and right position), thus the SDDR does not represent a significant concern in WS#2. The baking jacket doors play an important role in this SDDR reduction between WS#1 and WS#2, considering the shielding material "sandwich" layer composition used, as shown in Fig. 43.

- The activation of the whole ISS components (Fig. 44) is responsible for 40–45% of the SDDR amount in WS#1 (both left and right), representing a significant induced activation contribution. In addition, the activation of only tenants vacuum extensions (both DMS and XRCS-Core) and closure plate (components highlighted in yellow in Fig. 44) contribute to around 17% of SDDR in WS#1.

Considering the comparison between the baseline configuration and the "dummy" DSM#2 cases ("ideal" – no radiation transport on central drawers and "full" – no penetrations as shown in Fig. 45) in terms of SDDR %variation, the following assessment can be done (in accordance with values shown in Table 4:

- Even preventing the neutron transport through the central drawing ("ideal" case), the SDDR reduction achieved is around 40–50% in WS#1. Any design optimisation that could be introduced with the aim to mitigate the penetrations on the DSM#2 ("full" case) structure would provide a maximum SDDR reduction of 40% in WS#1. The level of attenuation of the "full" shield is quite similar to the "ideal" case, thus confirming the effectiveness of improve the DSM#2 shielding performance. The streaming through the DSM#2 openings contributes of about ∼40% to the SDDR in WS#1. Remaining ∼60% is due to neutron streaming through DSM#1 and #3 channels, gaps between vacuum vessel and PP, and leakage through PP itself.

Considering the comparison between baseline configuration and the additional ISS shielding cases reported in Table 1, in terms of SDDR % variation in WS#1 (average left-right position), the following evaluations are stated (Table 5):

- The best SDDR reduction is achieved with the shielding case #4 (−30%), where 6% Vol. of Pb is used in the rear shielding panels.
- The lowest SDDR reduction is observed with shielding case #1a and #2a (−15%), where Al-Borated layer has been simulated with natural Boron composition.
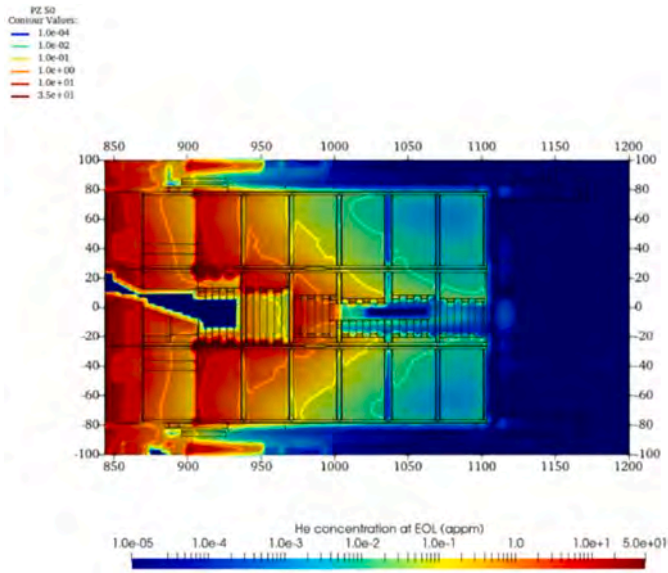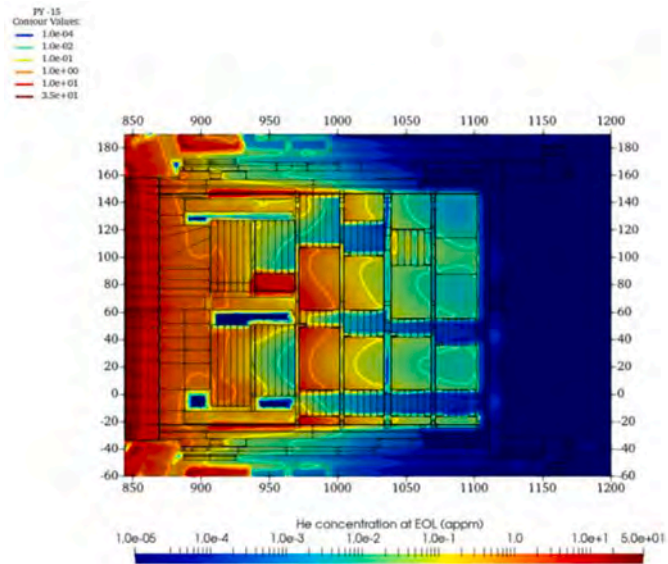
Fig. 34. Helium production at EOL in PZ 50.

Fig. 35. Helium production at EOL in PY −15 (DSM#2).

- Increasing the [10]B enrichment (up to 95%) in cases #1&2b the SDDR reduction increases (−20%).
- Both shielding cases #3&4 are characterized by an increased %Vol. of SS316L(N)-IG in all the panels compared to cases #1&2 a-b, which contributes to improve the SDDR %reduction.
- The only difference between case #3 and #4 is the implementation of Pb in the rear panels which contributes to improve the SDDR reduction from −25% (case#3) up to −30% (case #4).

6. Conclusions

MCNP model of ITER with EPP#2 has been produced starting from the original CAD. This has been simplified in order to perform an automatic conversion. Materials have been defined in agreement with the specifications and verified. It has then been integrated in the ITER C-

model used for past EPP#8 analyses for PDR. The integrated model has then been verified though lost particle check and stochastic volume calculation. The integration in the proper ITER sector to perform more reliable nuclear analysis including cross-talk with surrounding ports is foreseen for the next design phase of FDR.

The nuclear analyses have been performed with D1SUNED-v3.1.4 code to assess the nuclear quantities in the EPP#2 area during machine operations. Neutrons and prompt photons transport simulations have been performed to provide the nuclear heating on EPP #2 components, nuclear heating density maps, neutron and photon flux distribution maps, radiation induced damage on steel and copper, Tritium concentration and He- production. The neutron and photon flux and the nuclear heating are normalized to 500 MW of fusion power and the cumulated quantities (damage, helium and tritium production) are calculated at ITER EOL. Integral nuclear heating on components have been calculated with cell-based tallies. Neutron flux and spectra in specific location have been calculated with single voxel meshes. The other quantities have been calculated with $2 \times 2 \times 2$ cm^3 voxels meshes.

Neutron flux results about $2 \bullet 10^{14}$ n/cm^2/s at the FW and it decreases to more than $5 \bullet 10^8$ n/cm^2/s behind the CP. Significant neutron streaming is found around the PP, in correspondence of the six apertures (both on right and left side) of DMS DSM #1 and #3 and at the three central apertures of XRCS-Core of DSM #2. Behind these opening the neutron flux reaches values around $5 \bullet 10^9$ n/cm^2/s. The behavior of photon flux distribution is quite similar.

The calculated total nuclear power deposition on the three EPP#2 DSMs (not including PP structure), from neutrons and photons is 2.3 MW. Most of the power (about 80%) is deposited on the DFW structure. The DSM structure accounts for about 18% of the total power. The peak value for nuclear heating density in SS is around 7 W/cm^3 at the FW and decreases up to 10^{-5} W/cm^3 and below at the rear flange.

The design of the DSM#2 central SS shielding column (C1) has been revised during the PDR to remove nuclear heating hotspots on B$_4$C bricks.

The maximum damage in SS at EOL is 2.5 dpa at the FW that decreases up to 10^{-5} dpa at the closure plate regions, even if in some location it results greater than 10^{-4} dpa. This occurs, close to the streaming paths, because the damage is very sensitive to the high energy part of the spectrum.

The Tritium concentration at the ITER EOL shows the largest value of $4.4 \bullet 10^{-8}$ g/cm^3 in the B$_4$C of first shielding tray column. It decreases to approximately 10^{-11} g/cm^3 in the last shielding tray column. In general, the largest amount of tritium is produced inside Boron Carbide elements, while structural elements results in a minor amount of Tritium.

The largest amount of He production is found in the B$_4$C of the shielding trays in the first column and in the DFW mixture with a value of around 35–40 appm which decreases below 10^{-4} appm behind the closure plate.

The neutron flux and spectra, during operation, and, at the end of operation, the shutdown dose rate (SDDR) at 10^6 s at the end of SA2 scenario have been calculated with in "local" domain (i.e., excluding cross-talk with surrounding ports). The SDDR level will be greater in "global" domain due to cross-talk with surrounding ports (mainly from NB and upper port). Therefore, the results are underestimated especially in WS#2. Additional configurations have been studied to investigate the contribution of the central drawer and integrated systems, to the radiation field in the port interspace and to examine the consistent increase of the neutron streaming and SDDR in the port interspace. The neutron flux in PI area is greater than 10^8 n/cm^2/s in an area extending over about three meters from the closure plate. The neutron flux is much higher along the penetrations.

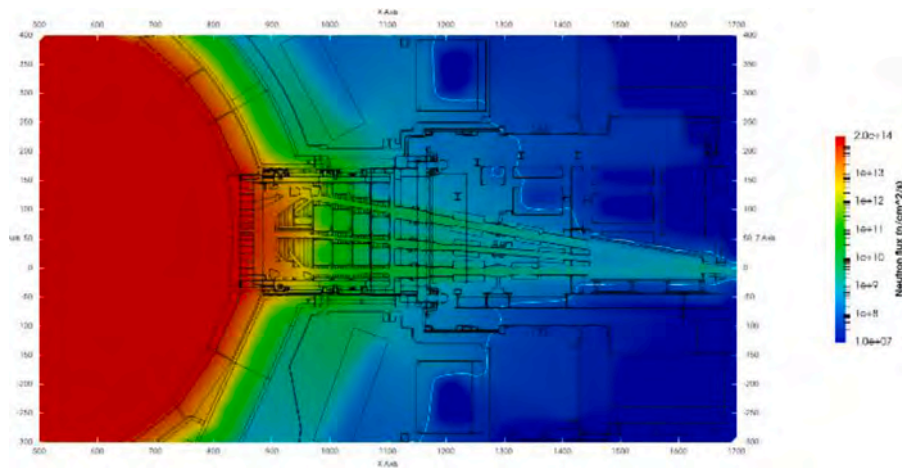The largest contribution in the SDDR originates from through the

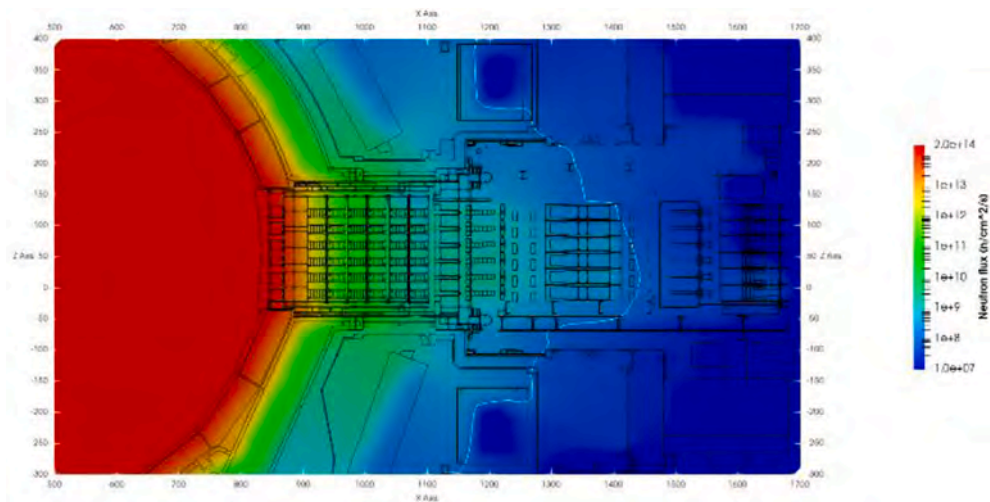**Fig. 36.** Neutron flux map at PY 0 along DSM#2. The white contour corresponds to 10^8 n/cm^2/s.

Fig. 37. Neutron flux map at PY 35 along DSM#1 and at PY −35 along DSM#3 (symmetrical behaviour). The white contour corresponds to 10^8 n/cm^2/s.
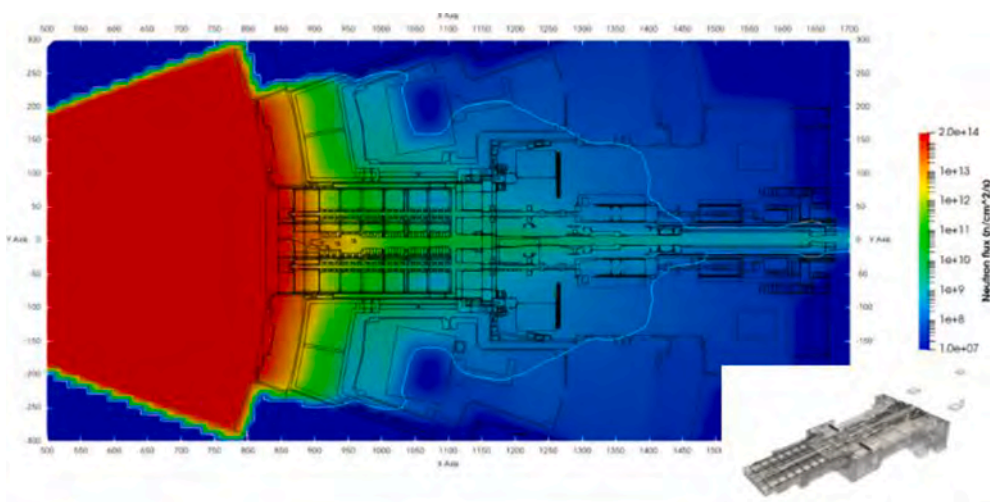

Fig. 38. Neutron flux map at PZ −8 (bottom section) along DSM#2 penetration. The white contour corresponds to 10^8 n/cm^2/s.
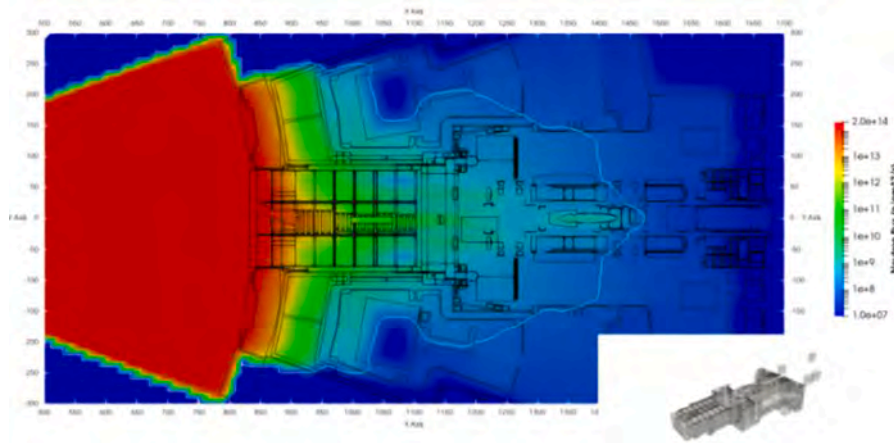
Fig. 39. Neutron flux map at PZ 50 middle port. The white contour corresponds to 10^8 n/cm^2/s.
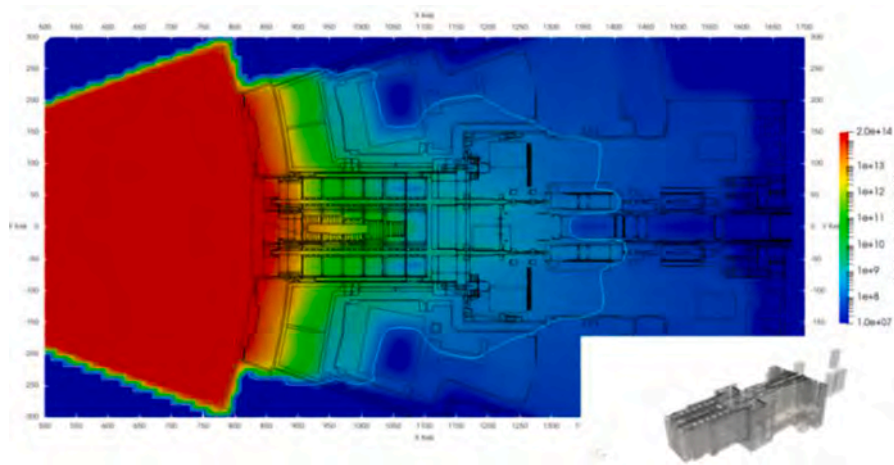

Fig. 40. Neutron flux map at PZ 120: along DSM#1, DSM#2 and DSM#3 penetrations. The white contour corresponds to 10^8 n/cm^2/s.

openings of XRCS-Core, the channels of DMS and from the gaps between vacuum vessel and PP. The level of attenuation of a DSM#2 shield without penetrations is similar to the ideal case (no radiation transport in DSM#2), thus confirming the appropriateness of the shielding design. It is necessary to implement shielding optimization even for the lateral drawers hosting DMS, the frame and the interface with VV. The backing doors have shown to have a great effect to reduce the radiation field between WS#1 and #2. The gaps between PP-Frame-VV also affect the PI environment and it is also needed to make parallel efforts to mitigate such effect.

The implementation of additional ISS shielding has shown that the best case in #4 with a SDDR reduction of −30%, achieved increasing the SS316L(N)-IG and Lead volume amount compared to the other shielding cases herein analyzed. In conclusion, this study aims to provide a complete and exhaustive overview of the nuclear analyses performed as support of the PDR of ITER Equatorial Port #2, highlighting both the main strengths and weaknesses of this design system in terms of radiations field impact. As such, one of the main guidelines recommended for the next design steps is the implementation of further large-scale shielding optimization strategies to reduce the neutron streaming in PI. This includes design optimization of in-vessel components combined with reduction of cross-talk among the drawers. Further efforts would be needed also to mitigate the streaming effect due to the gaps between PP-Frame-VV. Anyway, some ex-vessel shielding devices, as the baking jacket doors and heavy borated concrete shielding blocks are effective to reduce the radiation level in rear zone of the ISS.

CRediT authorship contribution statement

S. Noce: Conceptualization, Data curation, Formal analysis, Methodology, Visualization, Writing – original draft, Writing – review & editing. **R. Villari:** Conceptualization, Data curation, Formal analysis, Methodology, Supervision, Validation, Visualization, Writing – original draft. **A. Colangeli:** Conceptualization, Data curation, Formal analysis, Methodology, Validation, Visualization, Writing – original draft. **D. Flammini:** Conceptualization, Data curation, Formal analysis, Methodology, Validation, Visualization. **N. Fonnesu:** Supervision. **P. Gaudio:** Supervision. **M. Gelfusa:** Supervision. **E. Grasso:** Formal analysis, Supervision, Validation. **J. Guirao:** Supervision. **G. Mariano:** Conceptualization, Data curation, Formal analysis, Validation, Visualization, Writing – original draft. **F. Mercuri:** Formal analysis, Supervision, Validation. **F. Moro:** Supervision. **A. Previti:** Supervision, Writing – review & editing. **P. Shigin:** Supervision, Writing – review & editing. **S. Soro:** Supervision. **V.S. Udintsev:** Supervision, Writing – review & editing. **I. Wyss:** Conceptualization, Methodology.

Declaration of competing interest

The authors declare that they have no known competing financial interests or personal relationships that could have appeared to influence the work reported in this paper.
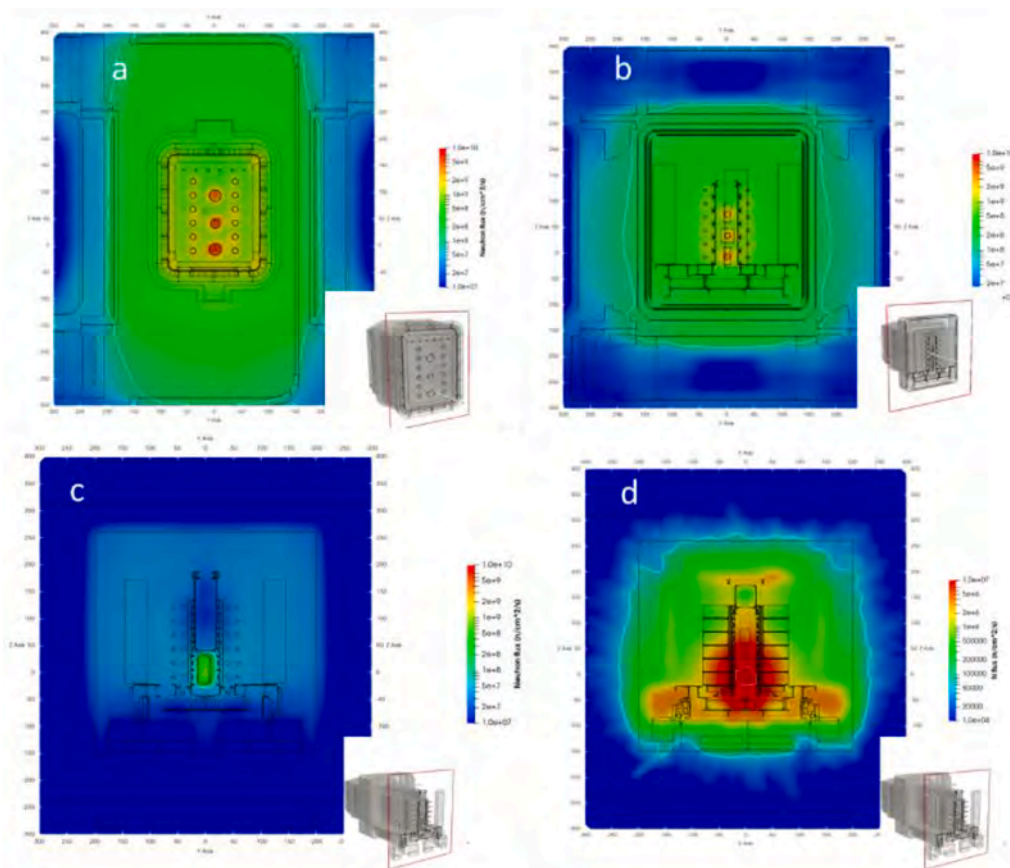
Fig. 41. Neutron flux maps at various toroidal-poloidal sections. PX 1125: behind closure plate (a); PX 1230: in PI- middle of WS#1 (b); PX 1560 in PI- middle of WS#2 (c); PX 1680: behind bio-shield plug (d). The white contour corresponds to 10^8 n/cm^2/s. The light-blue contour in (d) corresponds to $6 \cdot 10^4$ n/cm^2/s.
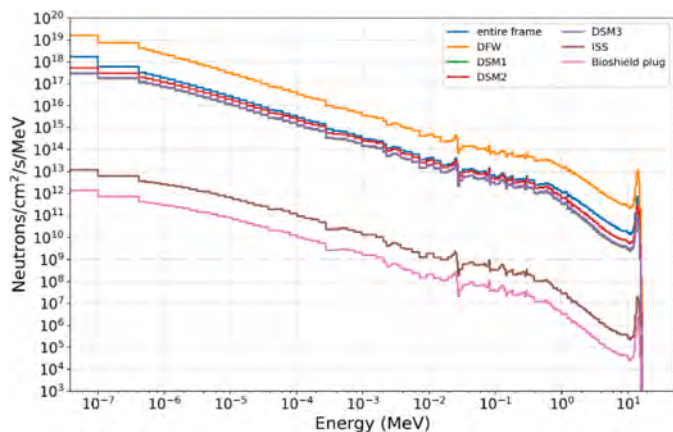

Fig. 42. Neutron spectra in EP#2 components (n/cm^2/s/MeV).

Table 2
Neutron flux in PI workstations (n/cm2/s) for 500 MW of fusion power.

Position	n/cm^2/s	Stat. Error (%)
WS#1-left	2.74E+08	1.2
WS#1-right	2.66E+08	1.2
WS#2-left	4.15E+07	1.2
WS#2-right	4.03E+07	1.5

Table 3
Average neutron flux in EP#2 components for 500 MW of fusion power.

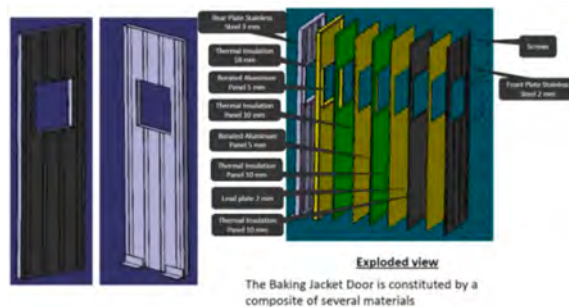| Component	n/cm^2/s	Stat. Error (%)
Entire frame and EPP#2	9.24E+12	0.3
DFW	1.16E+14	0.3
DSM#1	3.38E+12	0.5
DSM#2	6.04E+12	0.7
DSM#3	3.66E+12	0.5
ISS	3.31E+08	0.4
Bio-shield plug	3.79E+07	0.4

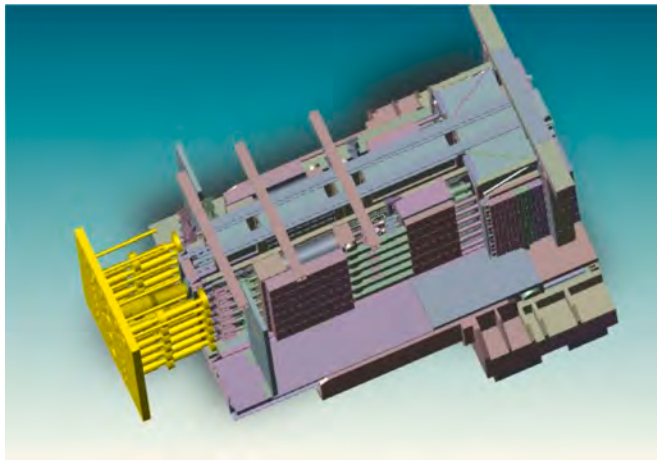**Fig. 43.** Baking Jacket Door layers and related materials.

Fig. 44. ISS components and highlights in yellow of the tenants' vacuum extensions (DMS and XRCS-Core) and closure plate.
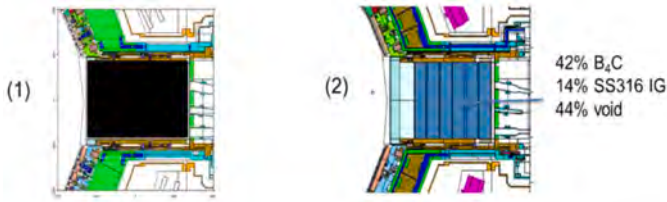

Fig. 45. Additional configurations examined to study the central drawer in-vessel components contribution: DSM#2 ideal shield (1) and DSM#2 full shield (2).

Table 4

WS#1 (left and right) SDDR %variation compared to the baseline DSM#2 with "ideal" and "full" DSM#2.

WS position	"IDEAL" SDDR%variation compared to baseline value	"FULL" SDDR%variation compared to baseline value
WS#1 L	−47%	−40%
WS#1 R	−41%	−39%

Table 5

SDDR %variation in WS#1 average left-right comparison between baseline configuration and several additional ISS shielding cases.

Configuration	ΔSDDR (%) – variation of SDDR in WS#1 (average Right – Left position) compared to the baseline configuration
Shielding Case#1a	−15%
Shielding Case#1b	−21%
Shielding Case#2a	−15%
Shielding Case#2b	−22%
Shielding Case#3	−25%
Shielding Case#4	−30%

Data availability

The authors are unable or have chosen not to specify which data has been used.

Acknowledgments

References

[1] P. Shigin. 55.Q2 - System Design Description (DDD) for Eq02, Private Communication, 2021.

[2] J. Guirao, et al., Standardized integration of ITER diagnostics equatorial port plugs, Fusion Eng. Des. 146 (2019) 1548–1552.

[3] R. Juarez, J. Guirao, A. Kolsek, et al., The use of the long modular diagnostics shield module to mitigate shutdown dose rates in the ITER diagnostics equatorial ports, Nucl. Fusion 58 (5) (2018).

[4] L.R. Baylor, C.C. Barbier, J.R. Carmichael, S.K. Combs, M.N. Ericson, N.D. Bull Ezell, P.W. Fisher, M.S. Lyttle, S.J. Meitner, D.A. Rasmussen, S.F. Smith, J. B. Wilgen, S. Maruyama, G. Kiss, Disruption mitigation system developments and design for ITER, Fusion Sci. Technol. 68 (2) (2015) 211–215, https://doi.org/10.13182/FST14-926.

[5] P. Beiersdorfer et al. 2010 J. Phys. B: at. Mol. Opt. Phys. 43 144008.

[6] P. Beiersdorfer, G.V. Brown, J. Clementson, J. Dunn, K. Morris, E. Wang, R. L. Kelley, C.A. Kilbourne, F.S. Porter, M. Bitter, R. Feder, K.W. Hill, D. Johnson, R. Barnsley, The ITER core imaging x-ray spectrometer: x-ray calorimeter performance, Rev. Sci. Instrum. 81 (10) (2010), https://doi.org/10.1063/1.3495789. PMID: 21034021.

[7] MCNPX-5 Monte Carlo Team, MCNP – A General Monte Carlo N-particle transport code overview and theory (Version 5, vol. I), Alamos Natl. Lab. (2003) 24. Report LA-UR-03-1987 (Revised 3.10.05).

[8] G. Pedroche, et al., Nuclear data for D1SUNED for the study of ITER planned in-situ maintenance dose scenarios, Fusion Eng. Des. 170 (2021) 112646.

[9] P. Sauvan, R. Juárez, G. Pedroche, J. Alguacil, J.P. Catalan, F. Ogando, J. Sanz, D1SUNED system for the determination of decay photon related quantities, Fusion Eng. Des. 151 (111399) (2020).

[10] M. Loughlin. Recommendation on Plasma Scenarios, Private Communication, 2009.

[11] www.spaceclaim.com.

[12] M. Loughlin. Instructions for Nuclear Analyses, Private Communication, 2015.

[13] R. Juarez. Neutronics guidelines for ITER Diagnostics Division, Private Communication, 2016.

[14] Y. Wu, F.D.S. Team, CAD-based interface programs for fusion neutron transport simulation, Fus. Eng. Des. 84 (2009) 1987–1992.

[15] P. Shigin. 55.Q2 - Nuclear Analysis Report - Port Plug, Private Communication, 2021.

[16] P. Shigin. 55.Q2 - Nuclear Analysis Report (PDR) - ISS and PCSS, Private Communication, 2021.

[17] D. Leichtle, B. Colling, M. Fabbri, R. Juarez, M. Loughlin, R. Pampin, E. Polunovskiy, A. Serikov, A. Turner, L. Bertalot, The ITER tokamak neutronics reference model C-Model, Fusion Eng. Des 136 (2018) 742–746.

[18] P. Shigin, 55.Q8 - Neutron shielding, nuclear loads and radiation damage calculations and analyses, Private Communication, 2018.

[19] R. Juarez, G. Pedroche, M.J. Loughlin, R. Pampin, P. Martinez, M. De Pietri, J. Alguacil, F. Ogando, P. Sauvan, A.J. Lopez-Revelles, A. Kolsek, E. Polunovskiy, M. Fabbri, J. Sanz, A full and heterogeneous model of the ITER tokamak for comprehensive nuclear analyses, Nat. Energy 6 (2) (2021) 150–157.

[20] FENDL-3.1d: fusion evaluated nuclear data library Ver.3.1d, https://www-nds.iaea.org/fendl/.

[21] M.C. White, "Further notes on MCPLIB03/04 and new MCPLIB63/84 Compton broadening data for all versions of MCNP5", LA-UR-12-00018 (2012) (Available at https://mcnp.lanl.gov/BUGS/la-ur-12.00018_mcw.pdf.

[22] F. Iannone, et al., CRESCO ENEA HPC clusters: a working example of a multifabric GPFS Spectrum Scale layout, in: Proceedings of the 2019 International Conference on High Performance Computing & Simulation (HPCS), Dublin, Ireland, 2019, pp. 1051–1052, https://doi.org/10.1109/HPCS48598.2019.9188135.

[23] S.W. Mosher et al., ADVANTG—An automated variance reduction parameter generator, ORNL/TM-2013/416, 2013 (https://info.ornl.gov/sites/publications/files/pub46035.pdf).

[24] E.A. Read, C.R.E. de Oliveira, A functional method for estimating DPA tallies in Monte Carlo calculations of light water reactors, in: Proceedings of the International Conference on Mathematics and Computational Methods Applied to Nuclear Science and Engineering, 2011.

[25] M.J. Norgett, M.T. Robinson, I.M. Torrens, A proposed method of calculating displacement dose rates, Nuclear Eng. Des. 33 (1975) 50–54.

[26] V. Barabash, Chemical composition and impurity requirements for materials, Private Communication, 2015.

[27] V. Barabash, Chemical compositions of materials representing the components included into basic model for nuclear analysis of ITER, Private Communication, 2014.

[28] M. Loughlin. C-model Terms of Use, Private Communication, 2016.